# nature materials

**Article** 

https://doi.org/10.1038/s41563-023-01510-7

# Resolving the polar interface of infinite-layer nickelate thin films

Received: 22 December 2021

Accepted: 14 February 2023

Published online: 27 March 2023



Berit H. Goodge  $oldsymbol{0}^{1,2}$ , Benjamin Geisler³, Kyuho Lee  $oldsymbol{0}^{4,5}$ , Motoki Osada  $oldsymbol{0}^{4,6}$ , Bai Yang Wang  $oldsymbol{0}^{4,5}$ , Danfeng Li  $oldsymbol{0}^{4,7,8}$ , Harold Y. Hwang  $oldsymbol{0}^{4,9}$ , Rossitza Pentcheva  $oldsymbol{0}^{3}$  & Lena F. Kourkoutis  $oldsymbol{0}^{1,2}$ 

Nickel-based superconductors provide a long-awaited experimental platform to explore possible cuprate-like superconductivity. Despite similar crystal structure and d electron filling, however, superconductivity in nickelates has thus far only been stabilized in thin-film geometry, raising questions about the polar interface between substrate and thin film. Here we conduct a detailed experimental and theoretical study of the prototypical interface between  $Nd_{1-x}Sr_xNiO_2$  and  $SrTiO_3$ . Atomic-resolution electron energy loss spectroscopy in the scanning transmission electron microscope reveals the formation of a single intermediate  $Nd(Ti,Ni)O_3$  layer. Density functional theory calculations with a Hubbard U term show how the observed structure alleviates the polar discontinuity. We explore the effects of oxygen occupancy, hole doping and cation structure to disentangle the contributions of each for reducing interface charge density. Resolving the non-trivial interface structure will be instructive for future synthesis of nickelate films on other substrates and in vertical heterostructures.

Superconducting hole-doped infinite-layer rare-earth nickelates,  $R \text{NiO}_2(R = \text{La}, \text{Nd}, \text{Pr})$ , are the most direct analogue so far to high critical temperature ( $T_c$ ) cuprates<sup>1-7</sup>, yet experimental measurements have already revealed key distinctions between nickelate and cuprate superconductors, including differences in hybridization, charge-transfer energy and pairing mechanism<sup>3,8,9</sup>. On the other hand, theoretical calculations have suggested that depletion of the rare-earth bands could result in Fermi surface reconstruction, which renders the nickelates cuprate-like despite these differences<sup>10,11</sup>. A more practical distinction between cuprate and nickelate systems so far, however, is the geometry of superconducting samples. Unlike bulk- and powder-synthesized cuprate compounds<sup>12–16</sup>, all reports of nickelate superconductivity to date<sup>1–6,17,18</sup> have been in thin-film geometries where the crystalline substrate (and in some cases, thin capping layer) provides epitaxial support for the infinite-layer phase<sup>19</sup>. The synthesis of bulk infinite-layer

samples has shown promising progress<sup>20</sup> but has yet to stabilize superconductivity.

This specificity raises questions about the interface between the substrate and nickelate film and its role in the observed superconductivity  $^{10,11,21-23}$ . In particular, a polar discontinuity should exist at an atomically abrupt, ideal interface between charge-neutral planes in the SrTiO\_3(001) substrate (Sr^2+O^2- and Ti^4+O^2\_2-) and charged planes in the film ( $R^{3+}$  and Ni^1+O^2\_2-)^{11,22}. In metallic films such as the nickelates, charge compensation at the interface may take the form of excess screening charge or displacements in the atomic lattice  $^{24}$ . These predictions hearken back to the discovery of superconductivity at the archetypal polar interface between insulating LaAlO\_3 and SrTiO\_3 $^{25,26}$ , raising the question of whether the observed transport in this new family of superconductors should be associated more closely with high- $T_{\rm c}$  cuprates or with exotic interface phenomena. Several studies have

<sup>1</sup>School of Applied and Engineering Physics, Cornell University, Ithaca, NY, USA. <sup>2</sup>Kavli Institute at Cornell for Nanoscale Science, Cornell University, Ithaca, NY, USA. <sup>3</sup>Department of Physics and Center for Nanointegration (CENIDE), University of Duisburg-Essen, Duisburg, Germany. <sup>4</sup>Stanford Institute for Materials and Energy Sciences, SLAC National Accelerator Laboratory, Menlo Park, CA, USA. <sup>5</sup>Department of Physics, Stanford University, Stanford, CA, USA. <sup>6</sup>Department of Materials Science and Engineering, Stanford University, Stanford, CA, USA. <sup>7</sup>Geballe Laboratory for Advanced Materials, Stanford University, Stanford, CA, USA. <sup>8</sup>Department of Physics, City University of Hong Kong, Kowloon, Hong Kong. <sup>9</sup>Department of Applied Physics, Stanford University, Stanford, CA, USA. ⊠e-mail: bhg37@cornell.edu; lena.f.kourkoutis@cornell.edu

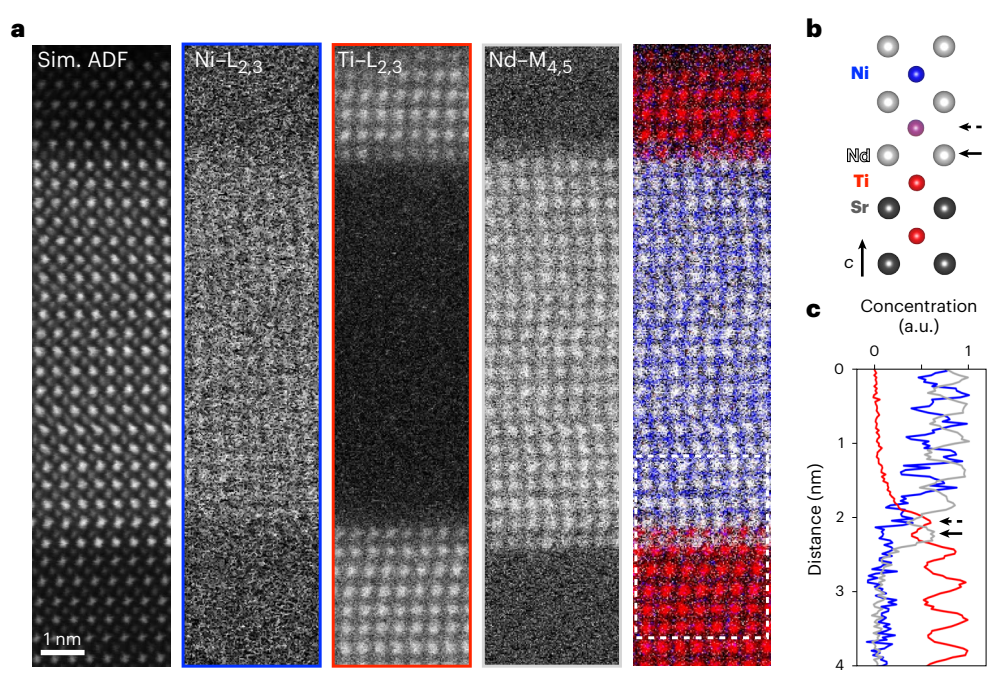


Fig. 1 | Intermediate atomic layer between nickelate film and substrate. a, Atomic-resolution elemental mapping by STEM-EELS reveals the formation of a single intermediate layer between an NdNiO $_2$  film and the SrTiO $_3$  substrate, resulting in **b**, cation stacking sequence across the interface represented schematically. The simultaneously recorded annular dark-field (Sim. ADF) image confirms the crystalline quality of the film in the mapped region.

c, Concentration profiles of Ni, Ti and Nd across the interface from the region marked by the dashed white box in a show that the intermediate layer is predominantly Ti with some Ni occupancy (dashed arrow). The first Nd-containing atomic plane (solid arrow) forms below the final Ti-containing atomic plane, disrupting the ideal SrTiO $_3$ -NdNiO $_2$  interface.

investigated possible effects at such a nickelate interface, predicting the formation of a high-carrier density two-dimensional electron gas  $(2{\rm DEG})^{11,21,23}$  or other electronic instability  $^{10}$ . These theoretical studies have furthermore indicated how subtly different interface reconstructions can have drastic effects on the electronic structure  $^{10,11,21-23}$ . While recent reports of superconducting nickelate thin films grown on  $({\rm LaAlO_3})_{0.3}({\rm Sr_2AlTaO_6})_{0.7}({\rm LSAT})^{18,27}$  demonstrate that superconductivity is not limited to the unique case of  $R{\rm NiO_2-SrTiO_3}$ , the weak polarity of LSAT (±0.18 electrons per 2D unit cell) leaves open the question of how such a discontinuity across the interface may impact the electronic structure of the nickelate film.

An atomic-scale understanding of both the chemical and electronic structures at the substrate—nickelate interface is therefore crucial. Are the interface and surface electronically distinct from the rest of the thin film? Is superconductivity in thin films representative of the bulk state? If the observed superconductivity is substantially impacted by interface effects, can it ever be realized in bulk-grown samples? As Botana et al. point out, "the first important question to clarify is which interface is actually realized in these systems"<sup>28</sup>.

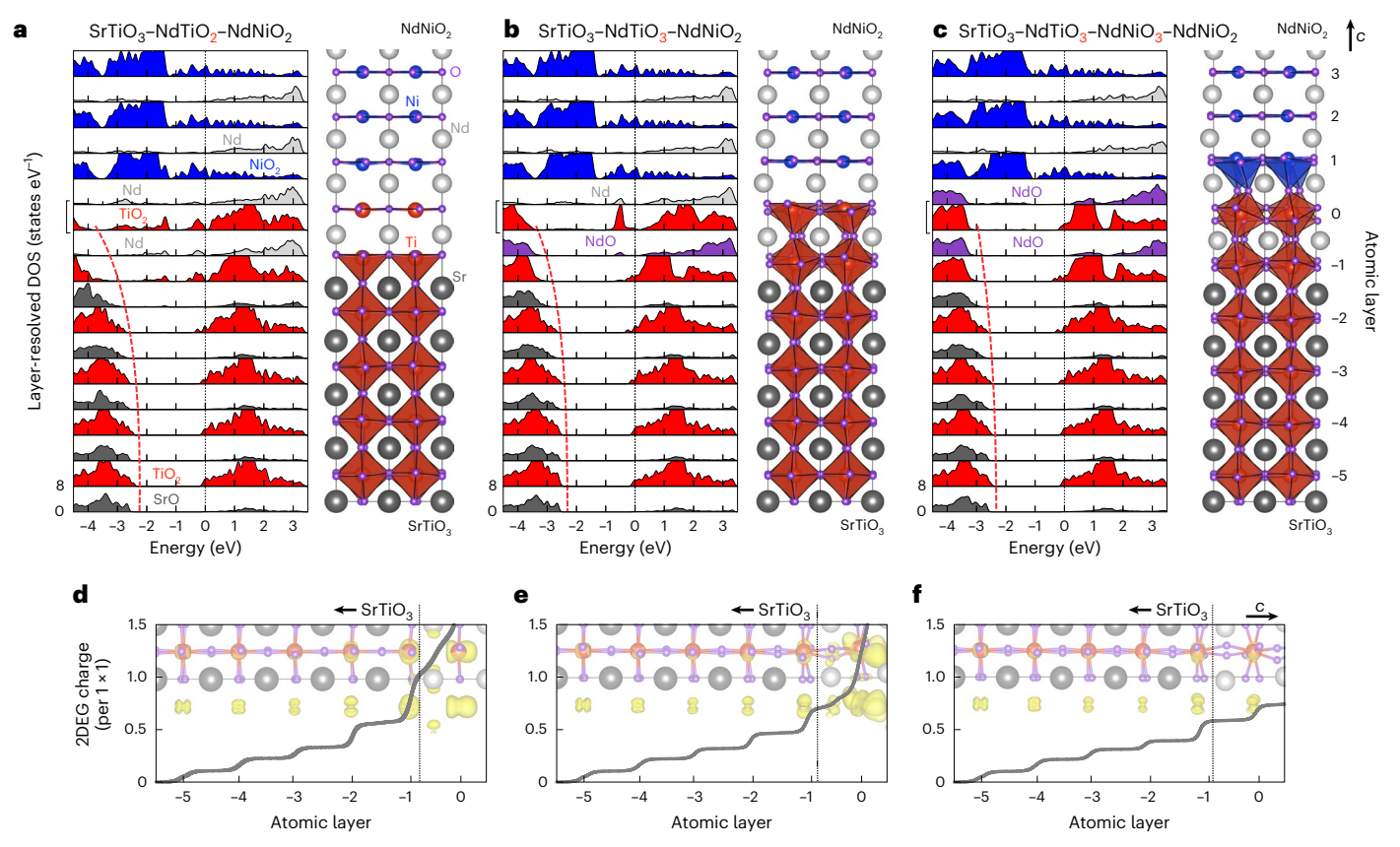
Here, we use electron energy loss spectroscopy (EELS) in the scanning transmission electron microscope (STEM) to resolve the atomic-scale lattice and electronic structure of the SrTiO $_3$ -NdNiO $_2$  interface, providing key insights into the role of the interface for observed superconductivity in infinite-layer nickelates. We reveal a single intermediate interface layer with distinct composition (Fig. 1). Through combined structural and spectroscopic measurements and comparison with density functional theory calculations with a Hubbard Uterm (DFT + U), we identify this layer as Nd(Ti,Ni)O $_3$  and show that the experimentally observed interface structure effectively quenches the formation of an interface 2DEG. Systematic variation of the model interface disentangles contributions from the atomic stacking sequence, oxygen occupancy and lattice distortions. Together, experimental

 $results \, and \, theoretical \, calculations \, establish \, a \, realistic \, picture \, of \, this \, superconducting \, system.$ 

Throughout the rest of this work, we use 'interface' in reference to the full atomic system spanning from bulk-like SrTiO $_3$  in the substrate to bulk-like NdNiO $_2$  in the thin film, including the region of transition between the two. For clarity, we designate the single atomic layer of mixed cations the 'intermediate layer'. This atomic structure is distinct from other diffuse interface systems, which show broadened profiles of chemical intermixing across a heterointerface  $^{24,29-31}$ . Here, the cation profiles remain abrupt and show sharp transitions between atomic layers. Precise quantification of the relative amounts of Ti and Ni in the intermediate layer is complicated by the comparatively low scattering cross-section  $^{32}$  of the Ni–L $_{2,3}$  edge relative to the Ti–L $_{2,3}$  and Nd–M $_{4,5}$  edges as well as the radiation sensitivity of these nickelate films  $^9$ , but an integrated concentration profile across the interface indicates that the B-site cation stoichiometry in this layer is predominantly Ti, with some Ni occupancy.

Further elemental mapping shows that the intermediate layer forms during the perovskite-phase growth and is retained during the chemical reduction process to the infinite-layer phase (Supplementary Figs. 1 and 2). It is thus far observed in all nickelate films stabilized on SrTiO $_3$ , regardless of chemical (Sr) doping or rare-earth species (Supplementary Figs. 1-6) $^{4,6,9}$ , and has been observed in hundreds of measurements across more than 20 individual films. The same intermediate layer is also observed at the top interface in films which are capped with SrTiO $_3$  (Supplementary Figs. 2 and 6) $^\circ$ . The universality of these observations therefore suggests that this intermediate layer is not an artefact of very specific growth conditions but inherent within the system and that the complete structure of the atomic interface—including the intermediate layer—may help alleviate the polar discontinuity that would otherwise form at an abrupt interface $^{29}$ .

The impact of excess Ti in the intermediate layer on potential charge buildup is examined using DFT + *U*. Previous work has shown



 $\label{eq:constraints} \textbf{Fig. 2} | \textbf{Model interface charge accumulation. a-c}, \text{Optimized atomic} \\ \text{geometries and layer-resolved DOS for three distinct oxygen interface structures} \\ \text{between NdNiO}_2 \text{ and SrTiO}_3 (001), \text{ each consistent with the experimentally} \\ \text{observed cation structure assuming a perfect intermediate TiO}_2 \text{ layer which is} \\$ 

fully square-planar (a), partially coordinated (b) and fully coordinated (c). **d-f**, Visualization of the 2DEG electron density integrated from -0.7 eV to  $E_{\rm F}$  (yellow) and calculated accumulated 2DEG charge for the interface structures shown in  ${\bf a-c}$ , respectively.

that while an abrupt interface between SrTiO<sub>3</sub> and NdNiO<sub>2</sub> should host a high carrier density 2DEG, a single layer of perovskite NdNiO<sub>3</sub> may be sufficient to prevent its formation<sup>11</sup>. We therefore explore the effect of oxygen occupancy across the experimentally observed interface. taking into account the intermediate layer (Fig. 2). Atomic layers are indexed from the intermediate NdTiO<sub>2</sub> layer 0, with each BO<sub>2</sub> plane increasing (decreasing) by integer values into the film (substrate). The AO and A planes are labelled by medial half-integers. We initially neglect any Ni in the intermediate layer and begin with the simplest models which approximate the observed cation stacking by using a TiO<sub>2</sub> plane in layer 0. Layer-resolved densities of states (DOS) are calculated for each atomic plane for three cases of oxygen occupancy: an abrupt transition from perovskite to infinite layer such that all Nd-containing planes are solely Nd and devoid of oxygen (Fig. 2a), a single NdO plane between the SrTiO<sub>3</sub> and intermediate TiO<sub>2</sub> plane such that no Ni-containing planes have perovskite-like octahedral coordination (Fig. 2b) and a full perovskite NdTiO<sub>3</sub> intermediate layer followed by infinite-layer NdNiO<sub>2</sub> such that the first Ni-containing plane is partially coordinated (Fig. 2c).

The DFT + U calculations demonstrate how excess interface charge depends strongly on oxygen stoichiometry. The first two cases in particular show pronounced band bending, especially in the substrate. Each of the structures shows a finite occupation of Ti 3d states, particularly  $d_{xy}$  orbitals. The total charge of the 2DEG, calculated by progressively integrating the states between -0.7 eV and the Fermi energy ( $E_F$ ), is comparatively smallest for the SrTiO<sub>3</sub>-NdTiO<sub>3</sub>-NdNiO<sub>3</sub>-NdNiO<sub>2</sub> interface in Fig. 2c. In all cases, however, the excess charge is localized and suggests that the Ti

valence in the intermediate layer is considerably modified toward 3+ rather than 4+.

While the annular dark-field (ADF)-STEM collection geometry used in Fig. 1a is sensitive to heavy nuclei, annular bright-field–STEM imaging is required for imaging lighter elements, such as oxygen. Empty and filled apical oxygen sites in the infinite-layer and perovskite structures in the NdNiO $_2$  film and SrTiO $_3$  substrate, respectively, are indeed visible on either side of the interface (Supplementary Fig. 8). For robust determination of oxygen occupancy and local Ti valence at the intermediate layer, however, we again harness the combined high spatial and energy resolution of STEM–EELS.

In addition to elemental mapping, STEM–EELS provides the capability to measure local charge modulations and interface effects  $^{24,33}$ . Figure 3 shows atomically resolved high-energy resolution STEM–EELS spectra probing electronic states across the SrTiO $_3$ -NdNiO $_2$  interface. For display purposes, the vertical orientation of the interface has been inverted from Fig. 1, such that the SrTiO $_3$  substrate is on top and the growth direction (c axis) points down (Fig. 3a). Summed and background-subtracted spectra showing the energy loss near-edge structure of Ti–L $_{2,3}$  and O–K EELS edges at each atomic layer are plotted in Fig. 3b,c, respectively, with references shown in grey (Methods). The end-member spectra for SrTiO $_3$  and NdNiO $_2$  are consistent with 'bulk-like' measurements of both compounds  $^{8,9}$ ; spectra in the film are consistent with full oxygen reduction to the infinite-layer phase', while the substrate layers show no sign of induced oxygen vacancies  $^{34}$ , consistent with the high reduction energy of SrTiO $_3$  (refs. 10,11,35).

Intriguingly, the Ti–L<sub>2,3</sub> spectra show very little modification across the interface other than a reduction in overall intensity consistent

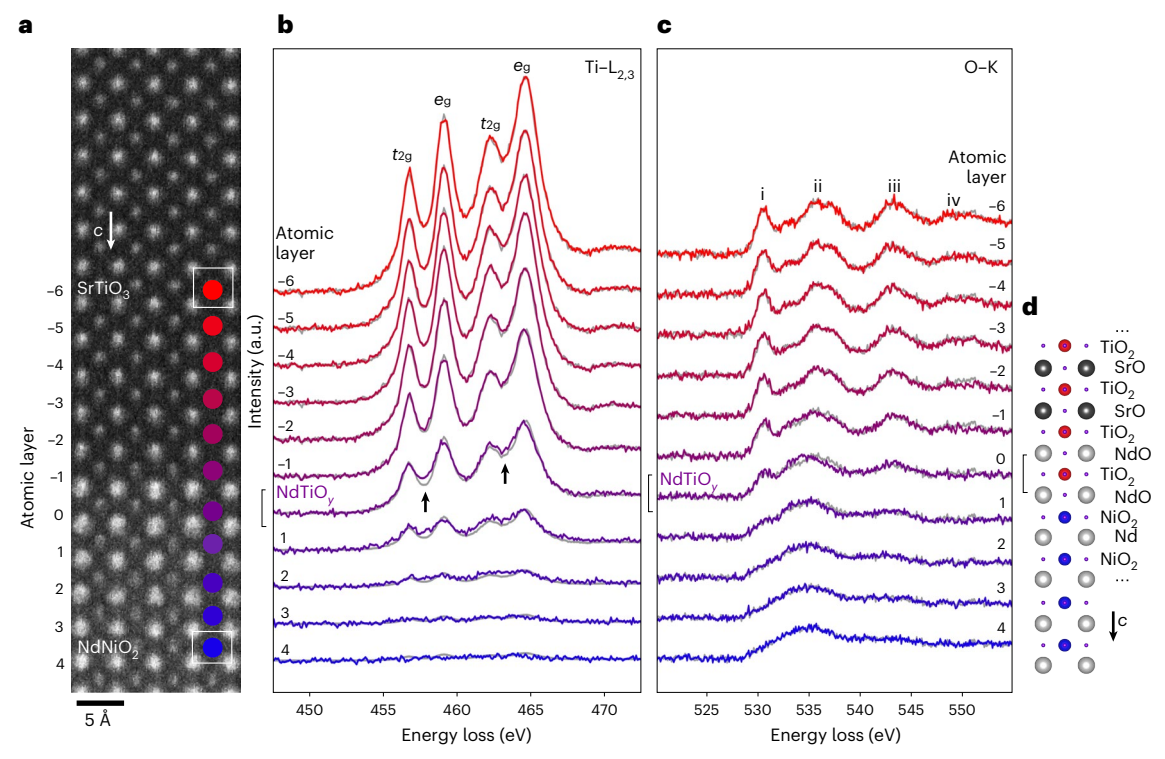
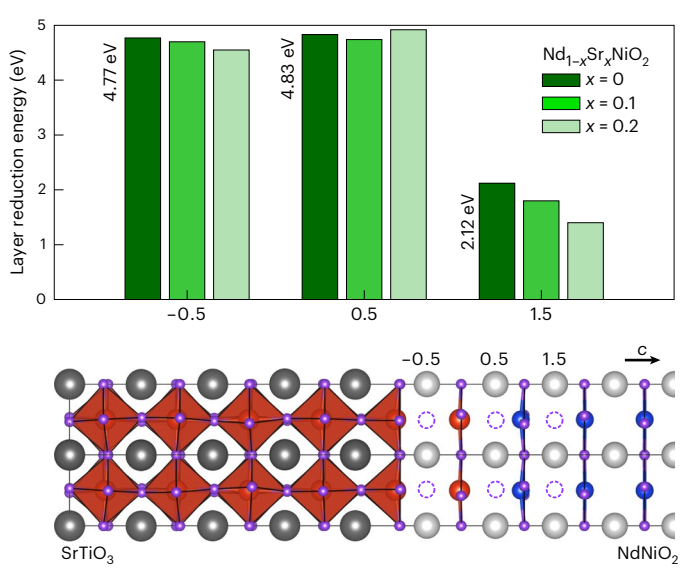


Fig. 3 | Experimental measurement of electronic structure across the interface. a, Representative HAADF–STEM image of the substrate–film interface with the atomic layers labelled according to the conventions used here. The growth direction is oriented downward as indicated by the arrow c. Coloured dots indicate the atomic layers for which each spectrum is a representative measurement (Methods). The white square and rectangle highlight the different

lattice symmetries of the perovskite SrTiO $_3$  substrate and infinite-layer NdNiO $_2$  film, respectively.  $\bf b$ , The Ti–L $_2$ 3 edge shows a minor filling between the  $e_g$  and  $t_{2g}$  peaks at the intermediate layer 0.  $\bf c$ , The O–K edge reflects the progression from bulk-like SrTiO $_3$  to NdNiO $_2$ . Also plotted are best-fit linear combinations of SrTiO $_3$  and NdNiO $_2$  references (grey).  $\bf d$ , Schematic representation of the observed interface structure with the atomic planes labelled.

with the observed stoichiometry (Fig. 1) and differences in the orbital bonding environment indicated by a subtle change to the  $L_{2,3}$  edge at the intermediate layer 0. There is no sign of notable  $\mathrm{Ti}^{3+}$  (ref. 33) at the intermediate layer. Instead, the small change in the  $L_{2,3}$  edge reflects changes to the coordination environment in the intermediate layer, which may arise from, for example, structural distortions introduced by the partial Ni occupancy so far neglected in our models but addressed in greater detail below. Probe tails and other beam-broadening effects give rise to the very weak  $\mathrm{Ti}-L_{2,3}$  edge signals, which persist in layers 1 and 2 despite the negligible Ti concentration in these layers measured by elemental mapping in Fig. 1.

By comparison, the O-K edge, which tracks chemical and electronic states as well as bonding environments in complex oxides 36,37, shows a more pronounced response across the interface. In layers -1 to 1, the O-K spectra show clear deviations from linear combinations of SrTiO<sub>3</sub> and NdNiO<sub>2</sub> references. At atomic layer -1, a broadening of the 'ii' peak, which tracks the A-site cation in complex oxides 37, reflects the proximity of this layer to both Sr and Nd cations. The intermediate layer 0 is fully surrounded by Nd-containing layers and resultingly, shows a more complete shift of this peak. Layer 1 can be almost entirely described by the NdNiO<sub>2</sub> reference (Supplementary Figs. 9 and 10), with only a small residual of peak 'i' remaining, possibly due to contributions from probe tails extending into layer 0. The stoichiometry of layer 1 suggests that the B sites are essentially fully occupied by Ni, with little or no Ti extending to this layer (Fig. 1a,c). Layers 2 and above are consistent with a fully reduced infinite-layer phase and Ni  $3d^9$  states<sup>9</sup>. Subtle variations in the higher-energy spectral features (for example, peak 'iv') reflect the metal 4sp bonding states, which are impacted by changes to atomic coordination and metal occupancy<sup>38-40</sup>, effects discussed in more detail below.



**Fig. 4** | **Impact of Sr doping on oxygen removal energy.** Calculated energy required to remove apical oxygens in the film cation layers across the interface for different levels of Sr doping in the  $Nd_{1-x}Sr_xNiO_2$  film, including undoped, lightly doped x = 0.10 and optimally doped x = 0.20.

We thus reconstruct an experimentally derived first-order model of the interface oxygen stoichiometry pictured schematically in Fig. 3d which matches the theoretical model in Fig. 2c.

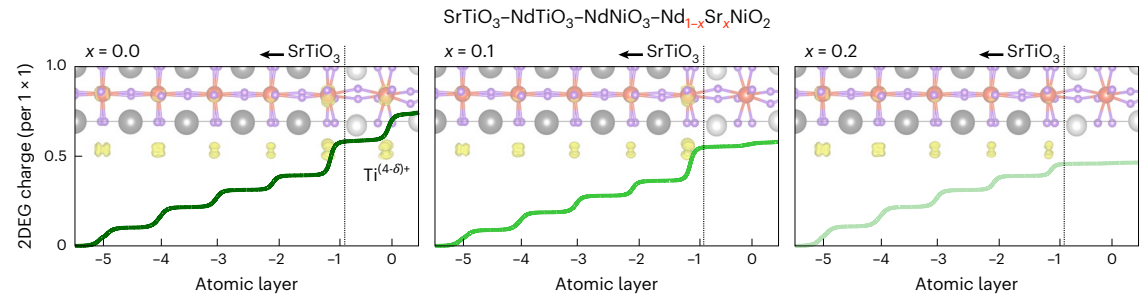


**Fig. 5** | **Impact of Sr doping on interfacial charge accumulation.** Accumulated interface charge in  $Nd_{1-x}Sr_xNiO_2$  films for systematic variation of Sr doping in the  $Nd_{1-x}Sr_xNiO_2$  film, including (left to right) undoped, lightly doped x = 0.10

and optimally doped x = 0.20, assuming perfect  $TiO_2$  stoichiometry in the intermediate layer (layer 0; Fig. 2c). Visualizations of the 2DEG electron density are shown in yellow.

DFT + U calculations further validate this structure by calculating the per-layer reduction energy required to remove apical oxygens from the perovskite phase of each layer across the interface. Figure 4 shows that the reduction energy near Ti is substantially higher than near Ni, qualitatively similar to previous calculations on related atomic interfaces  $^{10,11}$ . The finite concentration of Ti in the intermediate layer thus impedes the oxygen reduction from neighbouring AO planes.

We next consider the possible impact of Sr doping on both oxygen stoichiometry and the electronic structure of doped film interfaces with additional experiments and DFT + U calculations that explicitly include 10 and 20% Sr doping. As shown in Fig. 4, Sr doping in the nickelate film has only a modest impact on the reduction energy of oxygen in each atomic layer, confirming that the same oxygen structure is expected for all films, including those that fall within the superconducting dome<sup>4,6,41</sup>. Experimental EELS measurements of a doped Nd<sub>0.9</sub>Sr<sub>0.1</sub>NiO<sub>2</sub> film also show comparable structural and electronic evolution across both the substrate-film and film-capping layer interfaces (Supplementary Figs. 6 and 7). Figure 5 presents the impact of Sr doping on accumulated charge in the intermediate layer assuming the oxygen filling determined above. Sr doping is found to marginally reduce the interface charge as it introduces holes into the film, as observed by the decreasing levels of excess 2DEG charge from the undoped (x = 0%) to optimally doped (x = 20%) models. Even for relatively high Sr doping of 20%, however, the model suggests a clear tendency toward 2DEG formation near the intermediate laver.

The interface model presented in Figs. 2c and 3d thus fails to accurately reproduce the experimentally observed electronic structure of the intermediate layer. In particular, while the model suggests finite density of excess charge at the interface, experimental observations show no sign of a corresponding reduction in Ti valence. We, therefore, conclude that the model considered up to this point does not capture sufficient details of the system, and it is thus necessary to consider and account for the remaining parameter space, namely the observed but so far neglected Ni occupancy in the intermediate layer.

We finally consider in conjunction the role of Ni partial occupancy in the intermediate layer and more subtle structural distortions, which may play a role in accommodating the excess charge. Quantitative high-angle annular dark-field (HAADF)–STEM measurements track the c-axis lattice spacing in each unit cell across the interface (Fig. 6a). Figure 6b tracks the progression of the c-axis lattice constant measured between consecutive A-site planes observed experimentally and for two theoretical models, each consistent with expected values for SrTiO $_3$  and compressively strained NdNiO $_2$ <sup>41</sup> in the bulk-like regions. In experimental measurements, we observe a local expansion of the lattice across layer -1, between the final SrO and first NdO planes. Structural relaxations of the SrTiO $_3$ -NdTiO $_3$ -NdNiO $_3$ -NdNiO $_2$  interface obtained from DFT + U calculations reproduce a comparable

expansion of the -1 layer. The model, however, additionally shows an even larger c-axis expansion at the intermediate layer 0, which is not observed experimentally. Instead, by including Ni in the modelled intermediate layer, very close agreement is achieved between the experimental and theoretical structures. For the purposes of explicit DFT + Ucalculations, the model assumes a 50% Ti:50% Ni stoichiometry in the interface layer, although we note that the real stoichiometric ratio may differ somewhat. Still, the inclusion of Ni dramatically reduces the Nd-Nd distance (far beyond the Ti-Ni ionic radius difference) and very closely replicates the structure observed by HAADF-STEM imaging. We ascribe the remaining small discrepancies between experimental and theoretical measurements to subtleties which arise from the two methods, such as the ordered distribution of Ti and Ni in our models of the intermediate layer.

Electronically, this partial Ni occupancy almost entirely quenches the 2DEG. Figure 6e reveals that the excess charge is accommodated exclusively by the Ni–3  $d_{x^2-y^2}$  orbitals via Jahn–Teller distortions, which serve as a 'sponge' for excess charge and preserve Ti<sup>4+</sup>, as reflected in the projected DOS shown in Fig. 6c and comparison of integrated 2DEG charges in Fig. 6d. Additional DFT + U calculations which explicitly include 10 and 20% Sr in the nickelate show more complete suppression of the 2DEG charge in doped films (Supplementary Fig. 11). Despite this screening of the polar interface, the Nd–Sd states are still depleted in the layers contained within the model (Fig. 6c).

The combined results of our experimental and theoretical work paint a clear picture of the SrTiO<sub>3</sub>-NdNiO<sub>2</sub> interface, which has yet been the subject of much speculation. Rather than a strongly polar, abrupt atomic interface hosting a large 2DEG, the combined effects of atomic cation arrangement, subtle structural distortions and oxygen stoichiometry suppress the buildup of any excess charge. While these results demonstrate that the substrate-film interface does not itself host superconductivity, DFT + U results show reduced Nd 5d states within at least the first few atomic layers of the film, which suggest electronic reconstruction toward a more cuprate-like Fermi surface<sup>10,11,23</sup>. A similar Fermi surface reconstruction is not predicted for bulk NdNiO<sub>2</sub> modelled at the same lattice strain provided by the SrTiO<sub>3</sub> substrate<sup>11</sup>, so although it is not solely responsible for superconductivity, the atomic interface may yet have an important impact on the electronic structure of at least some volume of the film. This may be reflected in thickness-dependent studies<sup>42</sup>, but given the current materials challenges of synthesizing these films, it is difficult to rule out the impact of other extrinsic effects, such as a lattice or crystalline disorder.

While our results demonstrate that superconductivity in rare-earth nickelates is not driven by interfacial physics, it remains clear that the thin-film geometry plays an important role in the materials science of this system. We thus discuss two possible explanations which may contribute to the lack of superconducting bulk samples; (1) the substrate

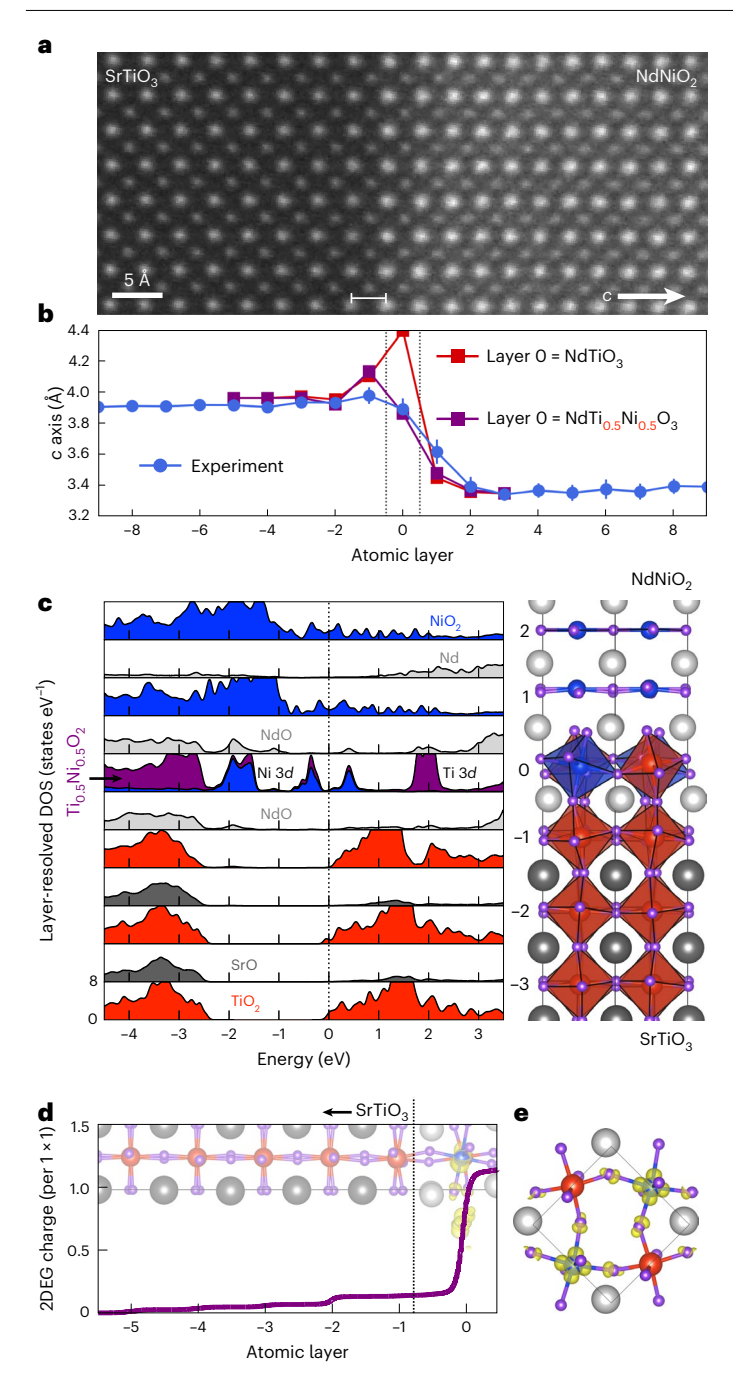


**Fig. 6** | **Full lattice and electronic structure of the nickelate-substrate interface. a**, HAADF-STEM image of a real interface used to measure the layer-resolved local c-axis lattice distance between rare-earth planes (for example, SrO-SrO or Nd-Nd). **b**, Comparison between experimental measurements (blue) and DFT + U results for a pure NdTiO $_3$  intermediate layer 0 (red; same as Fig. 2c) and 50% Ni substitution into the intermediate layer (purple). **c**, Layer-resolved DOS for the interface model with a mixed NdTi $_0$ sNi $_0$ sO $_3$  intermediate layer. The purple states at layer 0 represent Ti $_0$ sNi $_0$ sO $_2$ . The blue states in this layer are Ni 3d contributions. The states at -2 eV are purely of Ti-3d character. **d**, Accumulated 2DEG charge for the pure and mixed intermediate layer 'absorb' excess charge across the interface in the Ni 3dx $_2$ -y $_2$ states, thereby quenching the 2DEG in the SrTiO $_3$  substrate. Visualizations of the 2DEG electron density are shown in yellow.

provides important structural support during the chemical reduction process, or (2) some degree of lattice strain is necessary to stabilize superconductivity.

In the first case, previous studies have shown that stabilizing capping layers of  $SrTiO_3$  can dramatically improve the overall crystallinity of the reduced infinite-layer films<sup>19</sup>. It may therefore be necessary to explore other routes of oxygen reduction which will not require the mechanical support of a substrate. Recent measurements by resonant inelastic X-ray scattering suggest that similar considerations may also impact, for example, the stabilization of a charge density wave or magnon excitations in nickelate thin films, with some apparent correlation between the observation of these states with the presence or absence of a capping layer <sup>43–46</sup>. Again, however, it remains difficult to disentangle any intrinsic impact of a capping layer from the extrinsic effects of crystalline (dis-)order or lattice strain relaxation in the films.

An extreme example of the second explanation has been demonstrated in rutile RuO<sub>2</sub>, an otherwise metallic compound which can be made superconducting under very high epitaxial strain<sup>47</sup>. Applied and epitaxial strains have also been shown to enhance  $T_c$  in superconducting  $Sr_2RuO_4^{48-50}$ , while a recent report has shown enhancement of  $T_c$  by ~70% in Pr<sub>0.82</sub>Sr<sub>0.18</sub>NiO<sub>2</sub> thin films on SrTiO<sub>3</sub> under pressures beyond 12 GPa<sup>51</sup>. We note, however, that the native epitaxial strains in thin-film nickelates are somewhat lower (0.4% compressive for Nd<sub>0.8</sub>Sr<sub>0.2</sub>NiO<sub>2</sub> on SrTiO<sub>3</sub> versus anisotropic 2.3% tensile and 4.1% compressive strain for RuO<sub>2</sub>) and that the transition temperatures are appreciably higher (~5-15 K for nickelates, ~2 K for RuO<sub>2</sub>, up to ~3.5 K for Sr<sub>2</sub>RuO<sub>4</sub>). It will therefore be instructive to more thoroughly investigate the impact of strain on the nickelate system through either epitaxial strain or applied external strain. Some strain dependence may already be inferred through the differences in La, Pr and Nd thin films on SrTiO<sub>3</sub> (refs. 4,6,41), and epitaxial growth on different substrates, such as the recent stabilization of superconducting films on LSAT<sup>18,27</sup>, may offer a way to access further strain variation.

We identified a number of distinct physical mechanisms at work across the polar SrTiO<sub>3</sub>-NdNiO<sub>2</sub> interface, including both A- and B-site cation placements, lattice distortions and chemical doping. Guided by experimental STEM-EELS measurements and a systematic exploration of model systems by DFT + U calculations, we disentangle individual contributions of each variable within a wide parameter space. Our combined experimental and theoretical results provide insights for establishing a realistic picture of the infinite-layer nickelate superconductors. Despite the polar differences of the substrate and film, we have shown that a single intermediate atomic layer of Nd(Ti,Ni)O<sub>3</sub> prevents the formation of a 2DEG which could act as a channel for superconductivity. As superconducting films are realized on more substrates, it will be the subject of future work to explore the different characteristic interfaces that may form in each case. More broadly, the complex atomic structure of this interface should be instructive for future efforts to design nanoscale or few-layer heterostructures<sup>52</sup> and create predictive models of other strongly polar interfaces.

#### Online content

Any methods, additional references, Nature Portfolio reporting summaries, source data, extended data, supplementary information, acknowledgements, peer review information; details of author contributions and competing interests; and statements of data and code availability are available at https://doi.org/10.1038/s41563-023-01510-7.

#### References

- 1. Li, D. et al. Superconductivity in an infinite-layer nickelate. *Nature* **572**, 624–627 (2019).
- Zeng, S. et al. Phase diagram and superconducting dome of infinite-layer Nd<sub>1-x</sub>Sr<sub>x</sub>NiO<sub>2</sub> thin films. *Phys. Rev. Lett.* **125**, 147003 (2020)
- Gu, Q. et al. Single particle tunneling spectrum of superconducting Nd<sub>1-x</sub>Sr<sub>x</sub>NiO<sub>2</sub> thin films. Nat. Commun. 11, 6027 (2020).

- Osada, M. et al. A superconducting praseodymium nickelate with infinite layer structure. Nano Lett. 20, 5735–5740 (2020).
- Zeng, S. et al. Superconductivity in infinite-layer nickelate La<sub>1-x</sub>Ca<sub>x</sub>NiO<sub>2</sub> thin films. Sci. Adv. 8, eabl9927 (2022).
- Osada, M. et al. Nickelate superconductivity without rare-earth magnetism: (La,Sr)NiO<sub>2</sub>. Adv. Mater. 33, 2104083 (2021).
- Gao, Q., Zhao, Y., Zhou, X. & Zhu, Z. Preparation of superconducting thin films of infinite-layer nickelate Nd<sub>0.8</sub>Sr<sub>0.2</sub>NiO<sub>2</sub>. Chin. Phys. Lett. 38, 077401 (2021).
- Hepting, M. et al. Electronic structure of the parent compound of superconducting infinite-layer nickelates. *Nat. Mater.* 19, 381–385 (2020).
- Goodge, B. H. et al. Doping evolution of the Mott-Hubbard landscape in infinite-layer nickelates. *Proc. Natl Acad. Sci. USA* 118, e2007683118 (2021).
- Bernardini, F. & Cano, A. Stability and electronic properties of LaNiO<sub>2</sub>/SrTiO<sub>3</sub> heterostructures. J. Phys. Mater. 3, 03LT01 (2020).
- Geisler, B. & Pentcheva, R. Fundamental difference in the electronic reconstruction of infinite-layer versus perovskite neodymium nickelate films on SrTiO<sub>3</sub> (001). *Phys. Rev. B* 102, 020502 (2020).
- Bednorz, J. G. & Müller, K. A. Possible high T<sub>c</sub> superconductivity in the Ba-La-Cu-O system. Z. Phys. B Condens. Matter 64, 189–193 (1986).
- Wu, M.-K. et al. Superconductivity at 93 K in a new mixed-phase Y-Ba-Cu-O compound system at ambient pressure. *Phys. Rev. Lett.* 58, 908 (1987).
- Maeda, H., Tanaka, Y., Fukutomi, M. & Asano, T. A new high-T<sub>c</sub> oxide superconductor without a rare earth element. *Jpn. J. Appl. Phys.* 27, L209 (1988).
- Sheng, Z. & Hermann, A. Bulk superconductivity at 120 K in the Tl-Ca/Ba-Cu-O system. *Nature* 332, 138-139 (1988).
- Schilling, A., Cantoni, M., Guo, J. & Ott, H. Superconductivity above 130 K in the Hg-Ba-Ca-Cu-O system. *Nature* 363, 56-58 (1993).
- Pan, G. A. et al. Superconductivity in a quintuple-layer square-planar nickelate. Nat. Mater. 21, 160–164 (2022).
- Ren, X. et al. Strain-induced enhancement of T<sub>c</sub> in infinite-layer Pr<sub>0.8</sub>Sr<sub>0.2</sub>NiO<sub>2</sub> films. Preprint at https://arxiv.org/abs/2109.05761 (2022).
- Lee, K. et al. Aspects of the synthesis of thin film superconducting infinite-layer nickelates. APL Mater. 8, 041107 (2020).
- Puphal, P. et al. Topotactic transformation of single crystals: from perovskite to infinite-layer nickelates. Sci. Adv. 7, eabl8091 (2021).
- Zhang, Y. et al. Similarities and differences between nickelate and cuprate films grown on a SrTiO<sub>3</sub> substrate. *Phys. Rev. B* **102**, 195117 (2020).
- 22. He, R. et al. Polarity-induced electronic and atomic reconstruction at NdNiO<sub>2</sub>/SrTiO<sub>3</sub> interfaces. *Phys. Rev. B* **102**, 035118 (2020).
- Geisler, B. & Pentcheva, R. Correlated interface electron gas in infinite-layer nickelate versus cuprate films on SrTiO<sub>3</sub> (001). *Phys. Rev. Res.* 3, 013261 (2021).
- Mundy, J. A. et al. Visualizing the interfacial evolution from charge compensation to metallic screening across the manganite metal-insulator transition. *Nat. Commun.* 5, 3464 (2014).
- Ohtomo, A. & Hwang, H. Y. A high-mobility electron gas at the LaAlO<sub>3</sub>/SrTiO<sub>3</sub> heterointerface. *Nature* 427, 423–426 (2004).
- Reyren, N. et al. Superconducting interfaces between insulating oxides. Science 317, 1196–1199 (2007).
- Lee, K. et al. Character of the "normal state" of the nickelate superconductors. Preprint at https://arxiv.org/abs/2203.02580 (2022).

- 28. Botana, A. S., Bernardini, F. & Cano, A. Nickelate superconductors: an ongoing dialog between theory and experiments. *J. Exp. Theor. Phys.* **132**, 618–627 (2021).
- 29. Nakagawa, N., Hwang, H. Y. & Muller, D. A. Why some interfaces cannot be sharp. *Nat. Mater.* **5**, 204–209 (2006).
- Kourkoutis, L. F., Muller, D., Hotta, Y. & Hwang, H. Asymmetric interface profiles in LaVO<sub>3</sub>/SrTiO<sub>3</sub> heterostructures grown by pulsed laser deposition. *Appl. Phys. Lett.* 91, 163101 (2007).
- Kourkoutis, L. F., Song, J., Hwang, H. & Muller, D. Microscopic origins for stabilizing room-temperature ferromagnetism in ultrathin manganite layers. *Proc. Natl Acad. Sci. USA* 107, 11682–11685 (2010).
- 32. Egerton, R. Oscillator-strength parameterization of inner-shell cross sections. *Ultramicroscopy* **50**, 13–28 (1993).
- Ohtomo, A., Muller, D. A., Grazul, J. L. & Hwang, H. Y. Artificial charge-modulation in atomic-scale perovskite titanate superlattices. *Nature* 419, 378–380 (2002).
- 34. Zhou, X.-R. et al. Negligible oxygen vacancies, low critical current density, electric-field modulation, in-plane anisotropic and high-field transport of a superconducting Nd<sub>0.8</sub>Sr<sub>0.2</sub>NiO<sub>2</sub>/SrTiO<sub>3</sub> heterostructure. *Rare Metals* **40**, 2847–2854 (2021).
- 35. Sahinovic, A. & Geisler, B. Active learning and element embedding approach in neural networks for infinite-layer versus perovskite oxides. *Phys. Rev. Res.* **3**, L042022 (2021).
- de Groot, F. M. F. et al. Oxygen 1s x-ray-absorption edges of transition-metal oxides. Phys. Rev. B 40, 5715–5723 (1989).
- 37. Kourkoutis, L. F. et al. Atomic-resolution spectroscopic imaging of oxide interfaces. *Philos. Mag.* **90**, 4731–4749 (2010).
- 38. De Groot, F. et al. Oxygen 1s x-ray absorption of tetravalent titanium oxides: a comparison with single-particle calculations. *Phys. Rev. B* **48**, 2074 (1993).
- 39. Suntivich, J. et al. Estimating hybridization of transition metal and oxygen states in perovskites from O *K*-edge X-ray absorption spectroscopy. *J. Phys. Chem. C* **118**, 1856–1863 (2014).
- 40. Frati, F., Hunault, M. O. & De Groot, F. M. Oxygen k-edge X-ray absorption spectra. *Chem. Rev.* **120**, 4056–4110 (2020).
- Li, D. et al. Superconducting dome in Nd<sub>1-x</sub>Sr<sub>x</sub>NiO<sub>2</sub> infinite layer films. Phys. Rev. Lett. 125, 027001 (2020).
- Zeng, S. et al. Observation of perfect diamagnetism and interfacial effect on the electronic structures in infinite layer Nd<sub>0.8</sub>Sr<sub>0.2</sub>NiO<sub>2</sub> superconductors. *Nat. Commun.* 13, 743 (2022).
- 43. Lu, H. et al. Magnetic excitations in infinite-layer nickelates. *Science* **373**, 213–216 (2021).
- 44. Rossi, M. et al. A broken translational symmetry state in an infinite-layer nickelate. *Nat. Phys.* **18**, 869–873 (2022).
- 45. Krieger, G. et al. Charge and spin order dichotomy in  $NdNiO_2$  driven by the capping layer. *Phys. Rev. Lett.* **129**, 027002 (2022).
- Tam, C. C. et al. Charge density waves in infinite-layer NdNiO<sub>2</sub> nickelates. Nat. Mater. 21, 1116–1120 (2022).
- 47. Ruf, J. P. et al. Strain-stabilized superconductivity. *Nat. Commun.* **12**, 59 (2021).
- Hicks, C. W. et al. Strong increase of T<sub>c</sub> of Sr<sub>2</sub>RuO<sub>4</sub> under both tensile and compressive strain. Science 344, 283–285 (2014).
- 49. Steppke, A. et al. Strong peak in  $T_{\rm c}$  of  ${\rm Sr_2RuO_4}$  under uniaxial pressure. Science **355**, eaaf9398 (2017).
- 50. Nair, H. P. et al. Demystifying the growth of superconducting  $Sr_2RuO_4$  thin films. *APL Mater.* **6**, 101108 (2018).
- 51. Wang, N. N. et al. Pressure-induced monotonic enhancement of  $T_{\rm c}$  to over 30 K in the superconducting  ${\rm Pr_{0.82}Sr_{0.18}NiO_2}$  thin films. Nat. Commun. 13, 4367 (2022).
- 52. Ortiz, R. A. et al. Superlattice approach to doping infinite-layer nickelates. *Phys. Rev. B* **104**, 165137 (2021).

**Publisher's note** Springer Nature remains neutral with regard to jurisdictional claims in published maps and institutional affiliations.

Springer Nature or its licensor (e.g. a society or other partner) holds exclusive rights to this article under a publishing agreement with

the author(s) or other rightsholder(s); author self-archiving of the accepted manuscript version of this article is solely governed by the terms of such publishing agreement and applicable law.

@ The Author(s), under exclusive licence to Springer Nature Limited 2023

#### Methods

#### Sample growth and characterization

SrTiO<sub>3</sub> substrates were pre-annealed under standard conditions used to produce single-terminated surfaces 19,53,54. The infinite-layer NdNiO<sub>2</sub> on SrTiO<sub>3</sub> film presented here was synthesized under the 'high-fluence' laser imaging conditions described in ref. 19. An SrTiO<sub>3</sub> epitaxial capping layer was subsequently deposited<sup>1</sup>. Atomic force microscopy topography images show that a step-and-terrace surface is preserved throughout growth, suggesting well-controlled termination at each atomic layer during growth (Supplementary Fig. 12). After the growth, an annealing-based topochemical reduction was then employed to achieve the infinite-layer phase using CaH<sub>2</sub> as the reducing reagent under optimal conditions<sup>19</sup>. The transition from perovskite to infinite-layer phase can be quantified by the change in the out-of-plane lattice constant measured by X-ray diffraction  $\theta$ –2 $\theta$ symmetric scans of the film before and after reduction. The film used for experimental measurements in this work shows a reduced-phase lattice constant of 3.280 Å, indicating a complete transition to the fully reduced infinite-layer phase (Supplementary Fig. 13). Previous work<sup>9</sup> has shown that even in fully reduced films, local nanometre-scale pockets of incomplete oxygen reduction can remain. These regions can be identified spectroscopically by a residual pre-peak in the O-K edge near ~527 eV. We therefore pre-screen all regions of the sample before detailed measurements to avoid regions with signs of residual oxygen occupancy. All of the spectroscopic measurements included here have been acquired from regions which exhibit no such pre-peak and are, therefore, representative of the fully reduced phase.

#### Atomic-resolution STEM and EELS

Electron transparent STEM samples of each film were prepared on a Thermo Fisher Scientific Helios G4 UX focused ion beam using the standard lift-out method. Samples were thinned to <30 nm with 2-kV Ga ions, followed by a final polish at 1 kV to reduce the effects of surface damage. All specimens were stored in vacuum to prevent possible degradation in air.

HAADF-STEM was performed on an aberration-correction FEI Titan Themis at an accelerating voltage of 300 kV with a convergence angle of 30 mrad and inner and outer collection angles of 68 and 340 mrad, respectively. Elemental maps were recorded with a 965 GIF Quantum ER spectrometer and a Gatan K2 Summit direct electron detector operated in counting mode. Even in a well-optimized microscope environment, mechanical instabilities result in sample drift during measurements on the order of 6 Å min<sup>-1</sup> (ref. 55). Due to the longer per-pixel acquisition time required for spectroscopic measurements, the EELS maps and simultaneously acquired ADF images included here (Fig. 1 and Supplementary Figs. 1–5) represent total acquisition times of several minutes. While the overall lattice structure is preserved in each map (as clearly evidenced by the simultaneously acquired ADF accompanying each map), some distortions, such as stretching or skewing, in the resulting image are thus unavoidable given the average drift rate and total acquisition time. To ensure the utmost fidelity of the mapped elemental structure, no drift correction or other postprocessing which could introduce spatial artefacts has been applied to any of the elemental maps shown here. These maps and images are therefore not reliable for precise measurements of atomic structure and distortions. By comparison, the HAADF-STEM image presented in Fig. 6 and used for precision structural measurements is acquired as a series of 50 rapid-frame images (<1 s per frame), which are subsequently realigned and averaged by a method of rigid registration optimized to prevent lattice hops 56 to produce a high-signal-to-noise ratio, high-fidelity image of the atomic lattice. From this image, the position of every atomic column is identified using the DAOStarFinder photutils python package<sup>57</sup>. We subsequently measure the distance from each atomic column to the next along the vertical (growth) direction (that is, A site to A site as illustrated by the bracket in Fig. 6a) across a horizontal span of nearly 20 nm, as depicted in Supplementary Fig. 14. Figure 6b shows the average of these distances for each horizontal atomic layer. Error bars represent the s.d. of distances in each layer. In the substrate, the error bars are smaller than the markers.

Layer-resolved STEM-EELS across the substrate-film interface (Fig. 3) was performed with <15 pA probe current on a Nion UltraSTEM operated at 100 kV equipped with a high-stability stage, an Enfinium ER spectrometer and Quefina 2 camera. The effective energy resolution measured by the full width at half-maximum of the zero loss peak was -0.39 eV. Spectra were recorded as line profiles across the interface extending from the SrTiO $_3$  substrate into the NdNiO $_2$  film, with sampling density on the order of -1 pm per spectrum in several regions of the film. Integrating over -0.2 Å centred on each B site yields layer-resolved spectra for each data set, several of which have been summed to produce the high signal-to-noise series presented here. All spectra have been normalized by the total contributed exposure time for each.

Each spectrum is plotted over bulk references shown in grey, which are acquired during the same measurements from regions more than 10 unit cells from the interface. Ti–L $_{2,3}$  spectra are referenced against measurements from the SrTiO $_3$  substrate (Ti $^{4+}$ ). O–K spectra at each layer are compared with a best-fit linear combination of bulk-like references from SrTiO $_3$  and NdNiO $_2$  as determined by a least squares minimization  $C_1$  O $_{\rm SrTiO}_3$  +  $C_2$  O $_{\rm NdNiO}_2$ , where  $C_1$  and  $C_2$  are non-negative and O $_{\rm SrTiO}_3$  and O $_{\rm NdNiO}_2$  are the respective reference spectra. More details of the minimization are given in Supplementary Figs. 9 and 10.

#### **Density functional theory**

We performed first-principles calculations in the framework of density functional theory <sup>58</sup> as implemented in the Quantum ESPRESSO code <sup>59</sup>. The generalized gradient approximation was used for the exchange-correlation functional as parametrized in ref. 60. Static correlation effects were considered within the DFT + U formalism <sup>61,62</sup>, employing U = 4 eV on Ni and Ti sites in line with previous work <sup>11,23,63,64</sup>.

Wave functions and density were expanded into plane waves up to cutoff energies of 45 and 350 Ry, respectively (Supplementary Fig. 15). Ultrasoft pseudopotentials were used in conjunction with projector-augmented wave data sets 66. The Nd 4f electrons were consistently frozen in the core 11,23,35,63,67,68. We used a 12 × 12 × 1 Monkhorst–Pack **k**-point grid 69 and 5-mRy Methfessel–Paxton smearing 70 to sample the Brillouin zone. The ionic positions were accurately optimized, reducing ionic forces below 1 mRy a.u.  $^{-1}$ .

We modelled different infinite-layer nickelate–SrTiO $_3$ (001) interfaces with varying stoichiometries in superlattice geometry by using  $\sqrt{2}\,a \times \sqrt{2}\,a \times c$  supercells with two transition metal sites per layer to account for octahedral rotations, strained to the SrTiO $_3$  substrate lattice parameter a=3.905 Å. The symmetric supercells feature two identical interfaces on each side and comprise 18 monolayers (MLs) in total: 9.5 MLs of SrTiO $_3$  substrate, 1+1 MLs of NdTiO $_n$  (n=2,3) or mixed Nd(Ti $_{0.5}$ Ni $_{0.5}$ )O $_3$ , 1+1 MLs of NdNiO $_n$  and an additional 4.5 MLs of NdNiO $_2$ . The figures show half of each supercell. The supercell length c was optimized in each case. Hole doping was treated explicitly by substituting 10 and 20% of the Nd sites by Sr.

The layer by layer reduction energies <sup>11</sup> shown in Fig. 4 were calculated from the DFT + U total energies via  $E_i^f = E_{\text{layers} \geq i\text{reduced}} - E_{\text{layers} \geq i\text{-lreduced}} + \mu_0$ , where  $\mu_0 = \frac{1}{2}E_{0_2}$  models the oxygen-rich limit. Here, i = -0.5, 0.5, 1.5 enumerates the A-site layers from the SrTiO<sub>3</sub> substrate into the nickelate film.

# **Data availability**

The experimental data relevant to the findings of this paper have been deposited in the Platform for the Accelerated Realization, Analysis, and Discovery of Interface Materials (PARADIM) database at <a href="https://doi.org/10.34863/nf7t-jj61">https://doi.org/10.34863/nf7t-jj61</a>. Additional data, including that contained in Supplementary Information and results of the DFT + U calculations, are available upon reasonable request to the authors.

#### References

- Lippmaa, M. et al. Observation of SrTiO<sub>3</sub> step edge dynamics by real-time high-temperature STM. Appl. Surf. Sci. 130, 582–586 (1998).
- 54. Nishimura, T., Ikeda, A., Namba, H., Morishita, T. & Kido, Y. Structure change of TiO<sub>2</sub>-terminated SrTiO<sub>3</sub> (001) surfaces by annealing in O<sub>2</sub> atmosphere and ultrahigh vacuum. Surf. Sci. **421**, 273–278 (1999).
- Goodge, B. H., Bianco, E., Schnitzer, N., Zandbergen, H. W. & Kourkoutis, L. F. Atomic-resolution cryo-STEM across continuously variable temperatures. *Microsc. Microanal.* 26, 439–446 (2020).
- Savitzky, B. H. et al. Image registration of low signal-to-noise cryo-stem data. *Ultramicroscopy* 191, 56–65 (2018).
- Stetson, P. B. Daophot: a computer program for crowded-field stellar photometry. *Publ. Astron. Soc. Pac.* 99, 191 (1987).
- Kohn, W. & Sham, L. J. Self-consistent equations including exchange and correlation effects. Phys. Rev. 140, A1133 (1965).
- Giannozzi, P. et al. QUANTUM ESPRESSO: a modular and open-source software project for quantum simulations of materials. J. Phys. Condens. Matter 21, 395502 (2009).
- Perdew, J. P., Burke, K. & Ernzerhof, M. Generalized gradient approximation made simple. *Phys. Rev. Lett.* 77, 3865 (1996).
- Anisimov, V. I., Solovyev, I., Korotin, M., Czyżyk, M. & Sawatzky, G. Density-functional theory and NiO photoemission spectra. *Phys. Rev. B* 48, 16929 (1993).
- Cococcioni, M. & De Gironcoli, S. Linear response approach to the calculation of the effective interaction parameters in the LDA+U method. *Phys. Rev. B* 71, 035105 (2005).
- 63. Liu, J. et al. Heterointerface engineered electronic and magnetic phases of NdNiO<sub>3</sub> thin films. *Nat. Commun.* **4**, 2714 (2013).
- 64. Botana, A. A. & Norman, M. R. Similarities and differences between infinite-layer nickelates and cuprates and implications for superconductivity. *Phys. Rev. X* **10**, 011024 (2020).
- Vanderbilt, D. Soft self-consistent pseudopotentials in a generalized eigenvalue formalism. *Phys. Rev. B* 41, 7892 (1990).
- Blöchl, P. E. Projector augmented-wave method. *Phys. Rev. B* 50, 17953 (1994).
- Nomura, Y. et al. Formation of a two-dimensional single-component correlated electron system and band engineering in the nickelate superconductor NdNiO<sub>2</sub>. Phys. Rev. B 100, 205138 (2019).
- Lechermann, F. Late transition metal oxides with infinite-layer structure: nickelates versus cuprates. *Phys. Rev. B* 101, 081110 (2020).
- 69. Monkhorst, H. J. & Pack, J. D. Special points for Brillouin-zone integrations. *Phys. Rev. B* **13**, 5188 (1976).
- Methfessel, M. & Paxton, A. High-precision sampling for Brillouin-zone integration in metals. *Phys. Rev. B* 40, 3616 (1989).

### **Acknowledgements**

B.H.G. and L.F.K. acknowledge support from the Department of Defense Air Force Office of Scientific Research (FA 9550-16-1-0305: L.F.K.) and the Packard Foundation. This work made use of the Cornell Center for Materials Research Shared Facilities, which are supported through the NSF MRSEC Program (DMR-1719875; L.F.K.). The FEI Titan Themis 300 was acquired with support from NSF (NSF-MRI-1429155; L.F.K.), with additional support from Cornell University, the Weill Institute and the Kavli Institute at Cornell. The Thermo Fisher Helios G4 UX focused ion beam was acquired with support from the National Science Foundation Platform for Accelerated Realization, Analysis, and Discovery of Interface Materials (Cooperative Agreement DMR-1539918; L.F.K.). B.G. and R.P. acknowledge support from the German Research Foundation (DFG) within CRC/TRR 80 (107745057; R.P.). Projects G3 and G8 and computational time at magnitUDE were granted by the Center for Computational Sciences and Simulation of the University of Duisburg-Essen (DFG Grant INST 20876/209-1 FUGG; R.P.). The work at SLAC/Stanford is supported by the US Department of Energy, Office of Basic Energy Sciences, Division of Materials Sciences and Engineering (DE-AC02-76SF00515; H.Y.H.) and the Gordon and Betty Moore Foundation's Emergent Phenomena in Quantum Systems Initiative (GBMF9072 for synthesis equipment; H.Y.H.). M.O. acknowledges partial financial support from the Takenaka Scholarship Foundation.

#### **Author contributions**

B.H.G. and L.F.K. conceived of the project. L.F.K., R.P. and H.Y.H. supervised the research. B.H.G. and L.F.K. performed the electron microscopy, electron energy loss spectroscopy and corresponding data analysis. B.G. and R.P. performed the theoretical calculations and corresponding analysis. D.L. and M.O. grew and reduced the nickelate films. K.L., D.L., M.O. and B.Y.W. conducted materials and structural characterization. B.H.G., L.F.K., B.G. and R.P. wrote the paper. All authors discussed the results and revised the paper.

## **Competing interests**

The authors declare no competing interests.

#### **Additional information**

**Supplementary information** The online version contains supplementary material available at https://doi.org/10.1038/s41563-023-01510-7.

**Correspondence and requests for materials** should be addressed to Berit H. Goodge or Lena F. Kourkoutis.

**Peer review information** *Nature Materials* thanks the anonymous reviewers for their contribution to the peer review of this work.

**Reprints and permissions information** is available at www.nature.com/reprints.